# Mesoscale and Synoptic Scale Analysis of Narrow Cold Frontal Rainband during a Landfalling Atmospheric River in California during January 2021

**Xun Zou, Jason M. Cordeira, Samuel M. Bartlett, Brian Kawzenuk, Shawn Roj, Christopher Castellano, Chad Hecht, F. Martin Ralph**

CW3E, Scripps Institution of Oceanography, University of California San Diego, CA, USA

Corresponding authors: Xun Zou (x4zou@ucsd.edu) and Jason M. Cordeira (jcordeira@ucsd.edu)

Key Points

1. This atmospheric river caused sustained rainfall and short-duration precipitation related to a narrow cold-frontal rainband.
2. The narrow cold-frontal rainband is mainly driven by synoptic-scale quasi-geostrophic forcing for ascent and frontogenesis.
3. High-resolution modeling is necessary to improve the understanding and predictability of high-intense short-duration precipitation.

**Abstract**

Narrow cold-frontal rain bands (NCFR) often produce short-duration and high-intensity precipitation that can lead to flooding and debris flow in California (CA). On 27 January 2021, an atmospheric river (AR) associated with an intense surface cyclone made landfall over coastal northern CA, which featured a prominent NCFR. This study uses high-resolution West WRF simulations to accurately resolve the gap and core structure of the NCFR and provides reliable precipitation estimations, compensating for limitations of radar and satellite observations. This NCFR was supported by robust synoptic-scale quasi-geostrophic (QG) forcing for ascent and frontogenesis. It propagated southward from Cape Mendocino to Big Sur in 12 hours before stalling and rotating counter-clockwise in central/southern CA due to upstream Rossby wave breaking and amplifying upper-tropospheric trough. With the lower to middle tropospheric flow backed considerably to the south-southwest over the NCFR, the increase of the vertical wind shear caused the transition from parallel to trailing stratiform precipitation. The stall and pivot of the AR and NCFR led to intense rainfall with a 2-day precipitation accumulation greater than 300 mm over central CA. In addition, under the potential instability and frontogenesis, a moist absolutely unstable layer between 850 hPa to 700 hPa was captured at the leading edge of the NCFR, which indicated slantwise deep layer lifting and high precipitation efficiency. This study reveals synoptic-scale and mesoscale drivers of rainfall outside orographic lifting and reaffirms the importance of high-resolution numerical modeling for the prediction of extreme precipitation and related natural hazards.

**Plain Language Summary**

California often experiences short-duration, high-intensity rainfall associated with landfalling atmospheric rivers (ARs), which are long, thin corridors of moisture in the atmosphere. They can trigger post-fire debris flows, shallow landslides, and flash flooding. This study investigates both synoptic and mesoscale precipitation characteristics of a high-impact landfalling AR in January 2021 based on high-resolution weather model simulations. The landfalling AR was associated with an intense surface cyclone over the Northeast Pacific. It moved southward through 27 January prior to stalling along the central California Coast on 28 January. Due to the stalling and pivoting of the AR, the coast of central and southern California experienced a long-duration period of moderate precipitation, synoptic-scale forcing for ascent and short duration periods of intense precipitation. In addition, the intense precipitation along the cold front can be explained an effective dynamic lifting of a deep layer of atmosphere. At Las Tablas, California, this event produced >375 mm of rainfall and led to a post-fire debris flow ~30 km south of Big Sur. High-resolution weather modeling reveals the physical processes of precipitation and is necessary for the prediction of extreme precipitation and related natural hazards.

**Key words**: Narrow Cold-frontal Rain Band (NCFR), Atmospheric River (AR), Moist Absolutely Unstable Layer (MAUL), West WRF

## 1. Introduction

Atmospheric rivers (ARs) contain enhanced water vapor transport that may produce extreme precipitation, benefits to water supply, and challenges to water resources management across the Western U.S. (Ralph et al. 2004, 2019; Neiman et al. 2008; Kim et al. 2013). Extreme precipitation associated with landfalling ARs in California is often attributed to upslope flow of saturated air by a strong low-level jet stream (LLJ) in the various coastal and inland mountainous terrain (e.g., the Coastal Ranges, Sierra Nevada, and Transverse Ranges, among others). Orographic precipitation processes during landfalling ARs in California may also be accompanied by synoptic-scale processes associated with the parent mid-latitude cyclone and upstream upper-tropospheric trough, or mesoscale processes such as narrow cold frontal rainbands (NCFRs; e.g., Hobbs 1978; Matejka et al. 1980; Hecht and Cordeira 2017). The purpose of this study is to investigate both the synoptic and mesoscale precipitation characteristics of a high-impact landfalling AR (Fig. 1a) during January 2021 that featured a prominent NCFR that stalled and pivoted along the California Coast (Fig. 1b). This event produced >375 mm (>15 inches) of rainfall at Las Tablas, California (Fig. 1c) and led to a post-fire debris flow ~30 km south of Big Sur (Fig. 1d).

Many landfalling ARs in California feature short-duration, high-intensity rainfall associated with NCFRs that may, given their intensity and/or antecedent conditions, trigger post-fire debris flows, shallow landslides, and flash flooding (Cannon et al. 2020). These NCFRs may in turn jeopardize life, property, and public infrastructure (Cannon et al. 2018; Oakley et al. 2018a,b). A radar- and reanalysis-based climatology of NCFRs in southern California for 1995–2020 yielded 95 events (de Orla-Barile et al. 2022), including one in 2018 in Montecito (Oakley

et al. 2018a) that lead to 23 deaths, ~163 hospitalizations, and >$200 million USD in direct and indirect financial losses.

NCFRs in southern California often occur within synoptic-scale environments containing mobile upper-tropospheric troughs and landfalling ARs along the California coast, robust synoptic-scale quasi-geostrophic (QG) forcing for ascent, and a thermally direct lower-tropospheric ageostrophic circulation related to frontogenesis (Cannon et al. 2018, 2020). These NCFRs typically contain weak convective (buoyant) instability that contrasts with quasi-linear convective rainbands associated with squall lines (Geerts and Hobbs 1995; Cannon et al. 2018, 2020). Precipitation with NCFRs is typically shallow (<3 km deep) and forced by the advance of low-level cold air, convergence, and uplift of the lower-to-mid-tropospheric saturated air mass containing both the AR and LLJ (Eiras-Barca et al. 2018; see Fig. 6 from Cannon et al. 2018). Horizontal shear instability in the environment containing the AR and LLJ often leads to a scalloped gap-and-core structure that breaks the convective line into a series of non-precipitating and precipitating elements, respectively (Hobbs and Persson 1982; Browning 1986; Jorgensen et al. 2003). The three-dimensional structure of an NCFR is commonly recognized as an elongated band of strong reflectivity cores on radar (>40-50 dBZ) that are ~2–3 km in depth, ~3–5 km in width, and up to hundreds of kilometers in length (Browning 1986; Cannon et al. 2020).

The shallow convective structure of NCFRs in coastal California, when combined with coastal radar observation sites at elevated locations, results in challenges to observing their spatial and vertical structure using National Weather Service Weather Surveillance Radar-1988 Doppler (WSR-88D) radars (Jorgensen et al. 2003). These challenges lead to limitations in monitoring and forecasting short-duration high-intensity precipitation in locations susceptible to flash flooding or debris flows such as urban areas or locations with recent burn scars. While

recent advances in radar technology including the deployment of C-band and X-band radars as part of the Advanced Quantitative Precipitation Information (AQPI) network provide some localized observations of NCFRs (i.e., over the San Francisco Bay Area), many gaps remain, especially offshore. To overcome this observational gap, analysis of the NCFR in this study will employ a series of high-resolution (1-km) Weather Research and Forecasting (WRF) model simulations to assist in identifying the mechanisms associated with changes in synoptic-scale and mesoscale precipitation characteristics during the January 2021 landfalling AR. The following section 2 provides additional information on the data and methods used in this study and section 3 provides an overview of the landfalling AR and NCFR. Sections 4 and 5 provide a validation of the WRF model simulations against observations and a concluding discussion, respectively.

## 2. Data and Methods

The landfalling AR and NCFR in this study are analyzed using a version of the WRF model known as West-WRF (WWRF) that was developed to better describe AR characteristics and their associated precipitation patterns (Martin et al. 2018). The current study uses WWRF version 4.3.1 with a nested configuration that includes 9-km, 3-km, and 1-km outer, inner, and local domains over coastal California (Fig. 2a). The WWRF simulations are forced and bounded through nudging (every 3 hours only for domain 1) by the hourly ERA5 reanalysis dataset produced by the European Centre for Medium-Range Weather Forecasts (ECMWF; Hersbach et al. 2020). In total, four temporally overlapping 48-hour WWRF simulations were initialized at 0000 UTC on each day from 25 to 28 January 2021. Analyses in this study between 0000 UTC 26 January 2021 and 0000 UTC 29 January 2021 are derived from the 24-to-47-h simulation times of those four simulations (see Table S1) in a manner similar to Zou et al. (2021). The

physical parameterizations used in the WWRF simulation are listed in Table 1 and are identical to those used in a study of the 2019 NCFR event in southern California and other AR-related precipitation events (Cannon et al. 2018; Brandt et al. 2020).

The analysis of the landfalling AR and NCFR using WWRF is complemented by several observational and reanalysis datasets. Overland observations are provided by Automated Surface Observing System (ASOS; Fovell and Gallagher 2022) stations in California that primarily include hourly precipitation. Spatial analyses of different meteorological parameters are created using the ECMWF ERA5 dataset, Next Generation Weather Radar (NEXRAD) data, and precipitation information from the National Centers for Environmental Prediction (NCEP) Stage-IV quantitative precipitation estimates (Stage-IV QPEs). The Stage-IV QPEs consist of hourly precipitation data with 4-km grid spacing and can be used as a benchmark for moderate-to-heavy rainfall at certain locations, especially for convective precipitation (Nelson et al. 2016). Note that spatial mosaics of NEXRAD radar observations are obtained from the Multi-Radar Multi-Sensor (MRMS) project (Smith et al. 2016), which combines multiple radars from the network, surface observations and numerical weather prediction models.

To identify and quantify the strength and duration of the AR, the hourly integrated vapor transport (IVT) is calculated as follows:

$$IVT\ is\ defined\ as\ \left(\frac{1}{g}\int_{sfc}^{10} qu\mathrm{d}p\right)^2 + \left(\frac{1}{g}\int_{sfc}^{10} qv\mathrm{d}p\right)^2 \quad (1),$$

where g is the gravity acceleration constant (m $s^{-2}$), q is specific humidity (kg $kg^{-1}$), u and v are zonal and meridional wind (m $s^{-1}$), and d$p$ is the differential pressure (hPa). Quasi-geostrophic (QG) forcing is estimated based on advanced omega equation shown as follows (Hoskins et al. 1978):

$$Q = f\gamma\left[\left(-\frac{\partial V_g}{\partial x}\cdot\nabla\theta\right)i,\left(-\frac{\partial V_g}{\partial y}\cdot\nabla\theta\right)j\right] \qquad (2)$$

where γ is constant on isobaric surfaces, $V_g$ is the geostrophic velocity, and θ is potential temperature.

## 3. Results

### 3.1 AR and NCFR overview

The AR initially made landfall over coastal northern California at approximately 0000 UTC 27 January 2021 with a maximum IVT magnitude >600 kg $m^{-1}$ $s^{-1}$ that would later persist along the coast with IVT magnitudes >250 kg $m^{-1}$ $s^{-1}$ for 45 hours (Kawzenuk et al. 2023; Figs. S1 and 1a) – an AR2 according to the Ralph et al. (2019) AR scale. The landfalling AR was associated with an intense (<988 hPa) surface cyclone over the Northeast Pacific that propagated southward with the landfalling AR through 27 January prior to stalling along the central California Coast on 28 January. The AR contained a prominent NCFR that migrated southward from Cape Mendocino at ~0300 UTC 27 January 2021, to Santa Cruz at ~0900 UTC 27 January 2021, and Big Sur by ~1200 UTC 27 January 2021 prior to stalling through 28 January 2021 (Figs. 3b-d). The stalling of the NCFR was accompanied by a counter-clockwise rotation or pivot of the parent landfalling AR and the band of enhanced reflectivity resulting in prolonged high-intensity precipitation over the central California coastline near the Santa Lucia Range (Figs. 3b,d). The stall and pivot of the AR and NCFR over central California resulted in 2-day precipitation totals >300 mm with recurrence intervals spanning 5 to 110 years and 3-hour precipitation totals with recurrence intervals spanning 1 to 17 years (Table 2).

### 3.2 NCFR structure and precipitation

168 The structure of precipitation ahead of, along, and behind the NCFR changed before and
169 after it stalled and pivoted along the central California coast (Fig. 4). The observed gap-and-core
170 precipitation structure in KMUX NEXRAD radar imagery of the NCFR at 0600 UTC 27 January
171 2021 (Fig. 4e and f, inset) was simulated by the WWRF composite reflectivity as a scalloped line
172 with reflectivity values >45 dB*Z*. The NCFR initially also contained a relatively narrow region of
173 post-frontal trailing stratiform WWRF-derived composite reflectivity >30 dB*Z* and an extended
174 region of parallel stratiform enhanced reflectivity extending inland over central and northern
175 California at 0600 UTC 27 January 2021 (Fig. 4e). These structures occurred in association with
176 a well-defined cold-frontal boundary with coincident 10-meter wind shift (i.e., convergence) and
177 a strong southeast-to-northwest 2-m temperature gradient (Fig. 4a). Ahead of the NCFR,
178 southwest flow along the AR and LLJ at 850 hPa produced orographic precipitation in the
179 Coastal Mountains south of San Francisco through Big Sur (Figs. 4c,e). Following the stalling of
180 the AR and NCFR along the coast, the NCFR developed a larger region of post-frontal trailing
181 stratiform enhanced reflectivity offshore and over central and northern California at 0000 UTC
182 28 January 2021 (Fig. 4f). At this time, more southerly flow developed at 10 m in the cold air
183 behind the NCFR effectively decoupling the regions of strong low-level convergence and the
184 strong surface temperature gradient (Fig. 4b). Orographic precipitation continued in the
185 southwest flow along the AR and LLJ at 850 hPa ahead of the NCFR in coastal central
186 California (Figs. 4d,f).
187
188 3.3. Synoptic and mesoscale forcing mechanisms
189 The stalling and pivoting of the landfalling AR and NCFR occurred in association with
190 upstream Rossby wave breaking and an amplifying upper-tropospheric trough at 500 hPa over

191 the Northeast Pacific (Figs. 5a,b). Before the stall and upstream trough amplification, the parallel
192 stratiform region of enhanced precipitation proximal to the NCFR was collocated with a region
193 of QG forcing for ascent as illustrated by convergence of the Q-vector at 700 hPa at 0600 UTC
194 27 January 2021 (e.g., Hoskins et al. 1978; Hoskins and Pedder 1980) (Fig. 5c). Overland, it
195 appears that QG forcing for ascent occurred in association with geostrophic warm air advection
196 based on the orientation of geopotential heights and temperature in Fig. 5c and winds and
197 temperature in Fig. 4c, but offshore forcing for ascent was likely the result of differential
198 cyclonic vorticity advection by the geostrophic wind ahead of the existing upstream trough. In
199 both regions, the parallel orientation of the Q-vector with respect to potential temperature implies
200 that forcing should result in a net cyclonic rotation of the isentropes (Keyser et al. 1992)
201 consistent with the counter-clockwise pivot of the landfalling AR and NCFR. Following the stall
202 and pivot, the landfalling AR and NCFR remained juxtaposed with QG forcing for ascent related
203 to geostrophic warm air advection and differential cyclonic vorticity advection by the
204 geostrophic wind at 0000 UTC 28 January 2021 (Figs. 5b,d); however, the lower to middle
205 tropospheric flow at the surface, 850 hPa, and 700 hPa backed considerably to the south-
206 southwest over the NCFR (Figs. 4b, 4d, and 5b, respectively). The increase in vertical wind shear
207 likely influenced the transition from primarily parallel stratiform precipitation along the NCFR to
208 trailing stratiform precipitation behind the NCFR (Fig. 4f). This transition prolonged the duration
209 of intense precipitation along the California coast where the development of trailing stratiform
210 precipitation on 28 January 2021 fell in locations previously impacted by the NCFR and parallel
211 stratiform precipitation on 27 January 2021.

212 Precipitation along the NCFR was maintained by strong lower tropospheric frontogenesis
213 at 700 hPa that extended toward the south-southwest crossing the corresponding 700-hPa

geopotential height contours at 0600 UTC 27 January 2021 (Fig. 6a). In this way, geostrophic cold air advection was effectively forcing the southeast propagation of the NCFR along the California Coast leading to the uplift of the warm moist AR-related airmass ahead of the front. That airmass was also weakly potentially unstable based on positive values of the 1000-850-hPa equivalent potential temperature gradient (i.e., theta-e values decreasing with height; Fig. 6c). In this region where frontogenesis likely promoted the release of the potential instability, the WWRF model simulated a moist absolutely unstable layer (MAUL) extending from ~850 hPa to 700 hPa at the leading edge of the NCFR (Fig. 7). Note that previous research on MAULs suggests that these unstable layers are often just a few tens of kilometers in width, persist for up to 30 minutes, and occur in association with slantwise deep layer lifting (Bryan and Fritsch 2000, 2002). Frontogenesis along the NCFR became oriented parallel to the 700-hPa geopotential height contours during the stalling that occurred by 0000 28 January 2021 with a spatial decoupling of the frontal zone and regions of potential instability (Figs. 6b,d).

## 4. Comparisons between WWRF, ERA5, and observations

As expected, the 24-to-47-hour WWRF simulations bounded by and nudged with ERA5 reanalysis data provide similar synoptic-scale analyses (e.g., sea-level pressure and IVT magnitude) of the landfalling AR along the California Coast on 27-28 January 2021 (Fig. S1). Upon closer examination, comparison of the 3-hourly time series of IVT magnitudes from 26 to 29 January 2021 at Los Angeles (LAX) and San Francisco (SFO) illustrate that the WWRF produces slightly higher IVT magnitudes during the peak in AR intensity and/or slightly longer durations of intense IVT magnitudes, but is otherwise accurate with average biases of -3.3 kg $m^{-1}$ $s^{-1}$ and -5.7 kg $m^{-1}$ $s^{-1}$, respectively (Fig. S2).

Comparison of the WWRF precipitation with 71 overland station observations in California illustrates that the statewide average correlation coefficient (r) of 1-hour accumulated precipitation is 0.49 with 32.4% of stations containing an r-value >0.7 (Fig. S3a). The statewide average WWRF precipitation bias is 0.01 mm, but is on average greater than 0.2 across northern California (i.e., an over-prediction) and is less than -0.2 across southern California (i.e., an under-prediction). Time series of hourly precipitation from the WWRF and observations at SFO, LAX, and Auburn (AUN) illustrate that the WWRF is able to reasonably capture the timing and peaks in precipitation; however, WWRF tends to be ~1-2 hours too slow with the timing of short-duration, high-intensity precipitation related to the propagation of the NCFR at SFO and AUN on 27 January 2021 and at LAX on 28-29 January 2021 (Fig. S3b). Storm-total precipitation from the WWRF simulation as compared to the NCEP Stage-IV QPE for the 72-h period from 0000 UTC 27 January to 2300 UTC 29 January 2021 illustrates a similar pattern of precipitation (Figs. S3c, d); however, the WWRF simulations underestimated the 72-h accumulated precipitation in southern California in the Transverse ranges by up to 5 inches and overestimated precipitation in the northern Sierra Nevada (~40°N) by ~4 inches.

The WWRF accurately simulated the gap-and-core structure of the NCFR at 0600 UTC 27 January 2021 offshore that matched structural elements observed by MRMS as the NCFR propagated closer to the coast and within range of the coastal radar network on 27 January 2021 (Figs. 4e,f). In this case, the WWRF simulation provided a reasonable representation of the NCFR at ranges beyond the coastal radar network due to shallow convective structure and over-shooting of radar observations.

## 5. Concluding discussion

The landfalling AR in California in late January 2021 featured several mesoscale and synoptic-scale characteristics that promoted both a long duration (>24 hours) period of moderate precipitation related to sustained orographic and synoptic-scale forcing and short duration (<6-12 hour) periods of intense precipitation related to a NCFR. The locations that received the most precipitation, influenced by both the longest duration and highest intensity rainfall, were impacted by the stalling of the southward propagation of the landfalling AR and NCFR south of Big Sur in the Santa Lucia Range. The stalling of the landfalling AR was accompanied by a backing of IVT from west-southwest to south-southwest IVT directions and a counter-clockwise pivot of the NCFR driven by upstream Rossby wave breaking and upper-tropospheric trough amplification. The accompanied increase in vertical wind shear resulted in a transition from primarily parallel stratiform precipitation along the NCFR to trailing stratiform precipitation behind the NCFR that resulted in a prolonged period of precipitation in the location immediately poleward of the front.

The transition from parallel stratiform precipitation to trailing stratiform precipitation in the presence of increasing vertical wind shear is reminiscent of similar processes that occur within some squall lines and mesoscale convective systems (Parker and Johnson 2000). Note that in squall lines, the trailing stratiform precipitation is the result of environmental system-relative winds at all levels that are “front-to-rear” and typically occurs in association with evaporatively cooled low equivalent potential temperatures behind the front that drive the descent of a rear inflow jet toward the convective zone and forward propagation (Parker and Johnson 2000). That process is not observed in this case but is instead driven primarily by strong cold air advection (see Fig. 6a) as described by Geerts and Hobbs (1995) as a criterion to diagnostically differentiate between NCFRs and squall lines. The stalling of the NCFR into a narrow quasi-

stationary frontal rainband with associated southwest-to-northeast propagation of the trailing stratiform and core precipitation elements along the prevailing LLJ fits the extreme-rain-producing MCS archetype documented by Schumacher and Johnson (2005) as "training line - adjoining stratiform."

The mesoscale and synoptic-scale environment is similar to the NCFR event diagnosed over southern California by Cannon et al. (2020) including featuring weak potential stability released in the presence of frontogenesis and synoptic-scale forcing for ascent diagnosed via convergence of the Q-vector. The analysis of synoptic-scale forcing for ascent in Cannon et al. (2020) focused on the representation of the component of the Q-vector parallel to the lower tropospheric potential temperature gradient (i.e., pointing toward warm air) confirming the linkages across scales that support the presence of frontogenesis. Herein we focus instead on the representation of the component of the Q-vector perpendicular to the lower tropospheric potential temperature gradient (i.e., along the front with warm air on the right) identifying the processes that supported the stalling and pivoting of the landfalling AR and NCFR. The QG forcing for ascent associated with the analyzed Q-vector convergence, representative of both middle tropospheric geostrophic warm air advection and differential cyclonic vorticity advection by the geostrophic wind, also helps explain the observed stratiform precipitation structures along and behind the NCFR in addition to hydrometeor advection related to vertical wind shear discussed above. In both phases prior to and after the pivot, the best QG forcing for ascent associated with Q-vector convergence was collocated with the observed regions of stratiform precipitation (Fig. 7). This spatial overlap suggests that these regions of stratiform precipitation, including the orographic precipitation, may have been enhanced by seeder-feeder processes (e.g., Bergeron 1965; Kingsmill et al. 2016; Hecht and Cordeira 2017).

The development of a MAUL in this study is not unsurprising, given the presence of potential instability and frontogenesis, but their concurrence with landfalling ARs is not well documented. Environments favorable for the organization of mesoscale convective systems featuring MAULs (i.e., destabilization via layer lifting in the presence of saturation) typically contain high moisture, CAPE, and strong low-level wind shear such as the AR diagnosed in concert with two mesoscale convective systems that contributed to widespread flooding in Tennessee in May 2010 (Moore et al. 2012) that coincidentally also featured trailing line/adjoining stratiform precipitation structures. Note that the absence of significant CAPE during a landfalling AR does not imply a MAUL cannot occur, only that lifting of the potentially unstable airmass (i.e., drier air atop warmer/more moist air) resulted in differential cooling in the absence of or prior to convective mixing (Bryan and Fritsch 2000). The presence of a MAUL in this analysis is supported by the WWRF simulation in the absence of direct observations; however, rawinsonde observations featuring a MAUL during a landfalling AR in late February 2019 in Coastal California at Bodega Bay lend credibility to its presence in this event (Fig. S4). Interestingly, while orographic processes were well forecast by the WWRF model in that February 2019 event, the precipitation efficiency and microphysical complexity of the environment (e.g., robust saturated mesoscale forcing for ascent in concert with orographic precipitation in the region of the MAUL) were likely responsible for larger-than-forecast precipitation rates, higher precipitation efficiency, and resulting forecast errors in that event (not shown; personal communication F. Cannon, October 2021). Both the 2019 and 2021 events featuring apparent MAULs are candidates for future analysis beyond the scope of the current study.

In summary, the landfalling AR in California in late January 2021 featured both synoptic-scale and mesoscale precipitation processes related to QG forcing for ascent, upslope flow, a NCFR, potential instability and a MAUL, and likely the seeder-feeder mechanism. While previous studies of landfalling ARs demonstrate that differences in storm-total water vapor transport directed up the mountain slope contribute 74% of the variance in storm-total rainfall (Ralph et al. 2013), the current study provides some insight into the many physical processes that may comprise the remaining 26% of that variance and potentially an example of a complex event that would be a statistical outlier if added to the prior studies. The results of this study complement previous studies on AR-related NCFR events in California by Cannon et al. (2018, 2020) and reaffirm the importance of using high-resolution (~1 km) numerical modeling such as WWRF to analyze NCFRs and enhance situational awareness of short-duration high-intensity precipitation in the coastal environment along the U.S. West Coast. As in Cannon et al. (2020), we emphasize the need to study a larger sample of landfalling ARs containing NCFRs from both a phenomenological and numerical modeling perspective to further evaluate model deficiencies in the prediction of short-duration high-intensity precipitation, flash floods, and debris flows.

**Acknowledgements**

This research was supported by the State of California, Department of Water Resources Atmospheric Rivers Program Phase III (#4600014294) awards and the U.S. Army Corps of Engineers Forecast Informed Reservoir Operations (FIRO) Phase 2 (#W912HZ-19-2-0023) award at the Center for Western Weather and Water Extremes (CW3E) at the University of California, San Diego Scripps Institution of Oceanography. We are thankful for modeling support provided by Daniel Steinhoff (CW3E) and Matthew Simpson (CW3E).

## Open Research

ERA5 and ERA5 Land reanalysis data are available at the Copernicus Climate Change Service (C3S) Climate Date Store. Surface station observations are provided by Automated Surface Observing System (ASOS; Fovell and Gallagher 2022) stations archived at Iowa State University (https://mesonet.agron.iastate.edu/ASOS/). NEXRAD radar observations are obtained from the Multi-Radar Multi-Sensor (MRMS) project (Smith et al 2016; https://mrms.nssl.noaa.gov/qvs/product_viewer/). West WRF is developed at CW3E for weather and hydrological extremes in the western U.S. (https://cw3e.ucsd.edu/west-wrf/).

Reference List for Open Research:

Fovell, R. G., and A. Gallagher, 2022: An Evaluation of Surface Wind and Gust Forecasts from the High-Resolution Rapid Refresh Model. *Weather Forecast.*, **37**, 1049–1068, https://doi.org/10.1175/WAF-D-21-0176.1.

Smith, T. M., and Coauthors, 2016: Multi-Radar Multi-Sensor (MRMS) Severe Weather and Aviation Products: Initial Operating Capabilities. *Bull. Amer. Meteor.*, **97**, 1617–1630, https://doi.org/10.1175/BAMS-D-14-00173.1.

**References**:


Brandt, W. T., K. J. Bormann, F. Cannon, J. S. Deems, T. H. Painter, D. F. Steinhoff, and J. Dozier, 2020: Quantifying the Spatial Variability of a Snowstorm Using Differential Airborne Lidar. *Water Resour. Res.*, **56**, e2019WR025331, https://doi.org/10.1029/2019WR025331.

Browning, K. A., 1986: Conceptual Models of Precipitation Systems. *Weather Forecast.*, **1**, 23–41, https://doi.org/10.1175/1520-0434(1986)001<0023:CMOPS>2.0.CO;2.

Bryan, G. H., and M. J. Fritsch, 2000: Moist Absolute Instability: The Sixth Static Stability State. *Bull. Amer. Meteor.*, **81**, 1207–1230, https://doi.org/10.1175/1520-0477(2000)081<1287:MAITSS>2.3.CO;2.

Bryan, H., and M. Fritsch, 2002: The structure and dynamics of moist absolutely unstable layers in a simulated squall line [poster].

Cannon, F., C. W. Hecht, J. M. Cordeira, and F. M. Ralph, 2018: Synoptic and Mesoscale Forcing of Southern California Extreme Precipitation. *J. Geophys. Res. Atmos.*, **123**, 13,714-13,730, https://doi.org/10.1029/2018JD029045.

——, and Coauthors, 2020: Observations and Predictability of a High-Impact Narrow Cold-Frontal Rainband over Southern California on 2 February 2019. *Weather Forecast.*, **35**, 2083–2097, https://doi.org/10.1175/WAF-D-20-0012.1.

Cifelli, R., and Coauthors, 2022: Advanced Quantitative Precipitation Information: Improving Monitoring and Forecasts of Precipitation, Streamflow, and Coastal Flooding in the San Francisco Bay Area. *Bull. Amer. Meteor.*, **1**, https://doi.org/10.1175/BAMS-D-21-0121.1.

Eiras-Barca, J., A. M. Ramos, J. G. Pinto, R. M. Trigo, M. L. R. Liberato, and G. Miguez-Macho, 2018: The concurrence of atmospheric rivers and explosive cyclogenesis in the North

Atlantic and North Pacific basins. *Earth Syst. Dyn.*, **9**, 91–102, https://doi.org/10.5194/esd-9-91-2018.

Fovell, R. G., and A. Gallagher, 2022: An Evaluation of Surface Wind and Gust Forecasts from the High-Resolution Rapid Refresh Model. *Weather Forecast.*, **37**, 1049–1068, https://doi.org/10.1175/WAF-D-21-0176.1.

Geerts, B., and P. V. Hobbs, 1995: A squall-like narrow cold-frontal rainband diagnosed by combined thermodynamic and cloud microphysical retrieval. *Atmos. Res.*, **39**, 287–311, https://doi.org/10.1016/0169-8095(95)00018-6.

Hecht, C. W., and J. M. Cordeira, 2017: Characterizing the influence of atmospheric river orientation and intensity on precipitation distributions over North Coastal California. *Geophys. Res. Lett.*, **44**, 9048–9058, https://doi.org/10.1002/2017GL074179.

Hersbach, H., and Coauthors, 2020: The ERA5 global reanalysis. *Q. J. R. Meteorol. Soc.*, **146**, 1999–2049, https://doi.org/10.1002/qj.3803.

Hobbs, P. V., 1978: Organization and structure of clouds and precipitation on the mesoscale and microscale in cyclonic storms. *Rev. Geophys.*, **16**, 741–755, https://doi.org/10.1029/RG016i004p00741.

——, and P. O. G. Persson, 1982: The Mesoscale and Microscale Structure and organization of Clouds and precipitation in Midlatitude Cyclones. Part V: The Substructure of Narrow Cold-Frontal Rainbands. *J. Atmos. Sci.*, **39**, 280–295, https://doi.org/10.1175/1520-0469(1982)039<0280:TMAMSA>2.0.CO;2.

Hoskins, B. J., and M. A. Pedder, 1980: The diagnosis of middle latitude synoptic development. *Q. J. R. Meteorol. Soc.*, **106**, 707–719, https://doi.org/10.1002/qj.49710645004.

411 ——, I. Draghici, and H. C. Davies, 1978: A new look at the ω-equation. *Q. J. R. Meteorol. Soc.*,
412 **104**, 31–38, https://doi.org/10.1002/qj.49710443903.
413 Houze Jr., R. A., 2004: Mesoscale convective systems. *Rev. Geophys.*, **42**,
414 https://doi.org/10.1029/2004RG000150.
415 Jorgensen, D. P., Z. Pu, P. O. G. Persson, and W.-K. Tao, 2003: Variations Associated with
416 Cores and Gaps of a Pacific Narrow Cold Frontal Rainband. *Mon. Weather Rev.*, **131**,
417 2705–2729, https://doi.org/10.1175/1520-0493(2003)131<2705:VAWCAG>2.0.CO;2.
418 Keyser, D., B. D. Schmidt, and D. G. Duffy, 1992: Quasigeostrophic Vertical Motions
419 Diagnosed from Along- and Cross-isentrope Components of the Q Vector. *Mon. Weather*
420 *Rev.*, **120**, 731–741, https://doi.org/10.1175/1520-
421 0493(1992)120<0731:QVMDFA>2.0.CO;2.
422 Kim, J., D. E. Waliser, P. J. Neiman, B. Guan, J.-M. Ryoo, and G. A. Wick, 2013: Effects of
423 atmospheric river landfalls on the cold season precipitation in California. *Clim. Dyn.*, **40**,
424 465–474, https://doi.org/10.1007/s00382-012-1322-3.
425 Kingsmill, D. E., P. J. Neiman, and A. B. White, 2016: Microphysics Regime Impacts on the
426 Relationship between Orographic Rain and Orographic Forcing in the Coastal Mountains
427 of Northern California. *J. Hydrometeorol.*, **17**, 2905–2922, https://doi.org/10.1175/JHM-
428 D-16-0103.1.
429 Martin, A., F. M. Ralph, R. Demirdjian, L. DeHaan, R. Weihs, J. Helly, D. Reynolds, and S.
430 Iacobellis, 2018: Evaluation of Atmospheric River Predictions by the WRF Model Using
431 Aircraft and Regional Mesonet Observations of Orographic Precipitation and Its Forcing.
432 *J. Hydrometeorol.*, **19**, 1097–1113, https://doi.org/10.1175/JHM-D-17-0098.1.

Matejka, T. J., R. A. Houze Jr, and P. V. Hobbs, 1980: Microphysics and dynamics of clouds associated with mesoscale rainbands in extratropical cyclones. *Q. J. R. Meteorol. Soc.*, **106**, 29–56, https://doi.org/10.1002/qj.49710644704.

Moore, B. J., P. J. Neiman, F. M. Ralph, and F. E. Barthold, 2012: Physical Processes Associated with Heavy Flooding Rainfall in Nashville, Tennessee, and Vicinity during 1–2 May 2010: The Role of an Atmospheric River and Mesoscale Convective Systems. *Mon. Weather Rev.*, **140**, 358–378, https://doi.org/10.1175/MWR-D-11-00126.1.

Neiman, P. J., F. M. Ralph, G. A. Wick, Y.-H. Kuo, T.-K. Wee, Z. Ma, G. H. Taylor, and M. D. Dettinger, 2008: Diagnosis of an Intense Atmospheric River Impacting the Pacific Northwest: Storm Summary and Offshore Vertical Structure Observed with COSMIC Satellite Retrievals. *Mon. Weather Rev.*, **136**, 4398–4420, https://doi.org/10.1175/2008MWR2550.1.

Nelson, B. R., O. P. Prat, D.-J. Seo, and E. Habib, 2016: Assessment and Implications of NCEP Stage IV Quantitative Precipitation Estimates for Product Intercomparisons. *Weather Forecast.*, **31**, 371–394, https://doi.org/10.1175/WAF-D-14-00112.1.

Oakley, N. S., F. Cannon, R. Munroe, J. T. Lancaster, D. Gomberg, and F. M. Ralph, 2018a: Brief communication: Meteorological and climatological conditions associated with the 9 January 2018 post-fire debris flows in Montecito and Carpinteria, California, USA. *Nat. Hazards Earth Syst. Sci.*, **18**, 3037–3043, https://doi.org/10.5194/nhess-18-3037-2018.

Oakley, N. S., J. T. Lancaster, B. J. Hatchett, J. Stock, F. M. Ralph, S. Roj, and S. Lukashov, 2018b: A 22-Year Climatology of Cool Season Hourly Precipitation Thresholds Conducive to Shallow Landslides in California. *Earth Interact.*, **22**, 1–35, https://doi.org/10.1175/EI-D-17-0029.1.

de Orla-Barile, M., F. Cannon, N. S. Oakley, and F. M. Ralph, 2022: A Climatology of Narrow Cold-Frontal Rainbands in Southern California. *Geophys. Res. Lett.*, **49**, e2021GL095362, https://doi.org/10.1029/2021GL095362.

Pandya, R. E., and D. R. Durran, 1996: The Influence of Convectively Generated Thermal Forcing on the Mesoscale Circulation around Squall Lines. *J. Atmos. Sci.*, **53**, 2924–2951, https://doi.org/10.1175/1520-0469(1996)053<2924:TIOCGT>2.0.CO;2.

Parker, M. D., and R. H. Johnson, 2000: Organizational Modes of Midlatitude Mesoscale Convective Systems. *Mon. Weather Rev.*, **128**, 3413–3436, https://doi.org/10.1175/1520-0493(2001)129<3413:OMOMMC>2.0.CO;2.

Ralph, F. M., P. J. Neiman, and G. A. Wick, 2004: Satellite and CALJET Aircraft Observations of Atmospheric Rivers over the Eastern North Pacific Ocean during the Winter of 1997/98. *Mon. Weather Rev.*, **132**, 1721–1745, https://doi.org/10.1175/1520-0493(2004)132<1721:SACAOO>2.0.CO;2.

Ralph, F. M., T. Coleman, P. J. Neiman, R. J. Zamora, and M. D. Dettinger, 2013: Observed Impacts of Duration and Seasonality of Atmospheric-River Landfalls on Soil Moisture and Runoff in Coastal Northern California. *J. Hydrometeorol.*, **14**, 443–459, https://doi.org/10.1175/JHM-D-12-076.1.

Ralph, F. M., J. J. Rutz, J. M. Cordeira, M. Dettinger, M. Anderson, D. Reynolds, L. J. Schick, and C. Smallcomb, 2019: A Scale to Characterize the Strength and Impacts of Atmospheric Rivers. *Bull. Amer. Meteor.*, **100**, 269–289, https://doi.org/10.1175/BAMS-D-18-0023.1.

Schmidt, J. M., and W. R. Cotton, 1990: Interactions between Upper and Lower Tropospheric Gravity Waves on Squall Line Structure and Maintenance. *J. Atmos. Sci.*, **47**, 1205–1222, https://doi.org/10.1175/1520-0469(1990)047<1205:IBUALT>2.0.CO;2.

Schumacher, R. S., and R. H. Johnson, 2005: Organization and Environmental Properties of Extreme-Rain-Producing Mesoscale Convective Systems. *Mon. Weather Rev.*, **133**, 961–976, https://doi.org/10.1175/MWR2899.1.

Smith, T. M., and Coauthors, 2016: Multi-Radar Multi-Sensor (MRMS) Severe Weather and Aviation Products: Initial Operating Capabilities. *Bull. Amer. Meteor.*, **97**, 1617–1630, https://doi.org/10.1175/BAMS-D-14-00173.1.

Zou, X., D. H. Bromwich, A. Montenegro, S.-H. Wang, and L. Bai, 2021: Major surface melting over the Ross Ice Shelf part I: Foehn effect. *Q. J. R. Meteorol. Soc.*, **147**, 2874–2894, https://doi.org/10.1002/qj.4104.

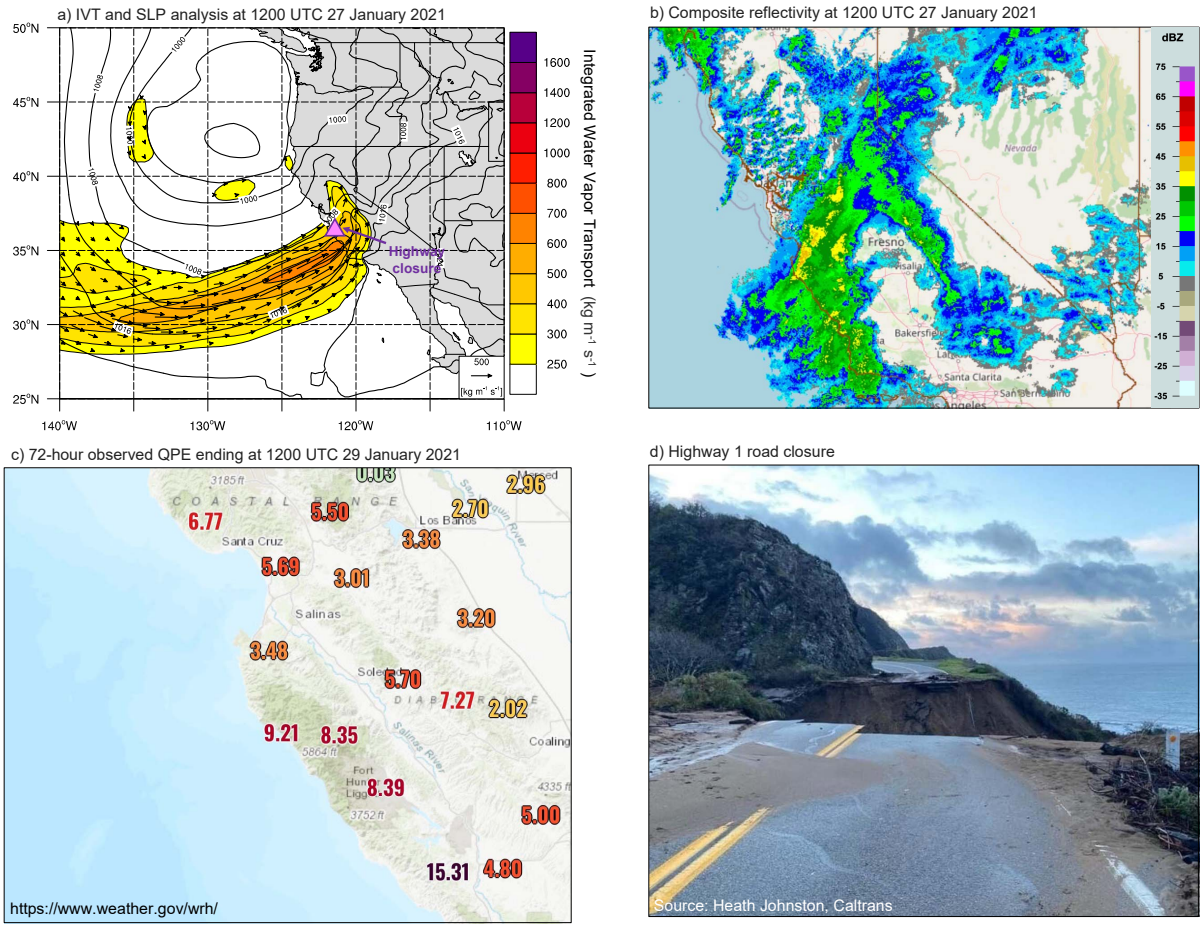


**Figure 1.** The overview of the 2021 NCFR event. a) Integrated vapor transport (IVT; filled contours and vectors; kg $m^{-1}$ $s^{-1}$ and mean sea level pressure (SLP; gray contours; hPa) at 1200 UTC 27 January from ERA5 reanalysis data. b) composite reflectivity from MRMS operational product viewer at 1200 UTC 27 January. c) 72-h observed precipitation (inches) from NWS network; d) Highway 1 closure near Big Sur caused by landslide.

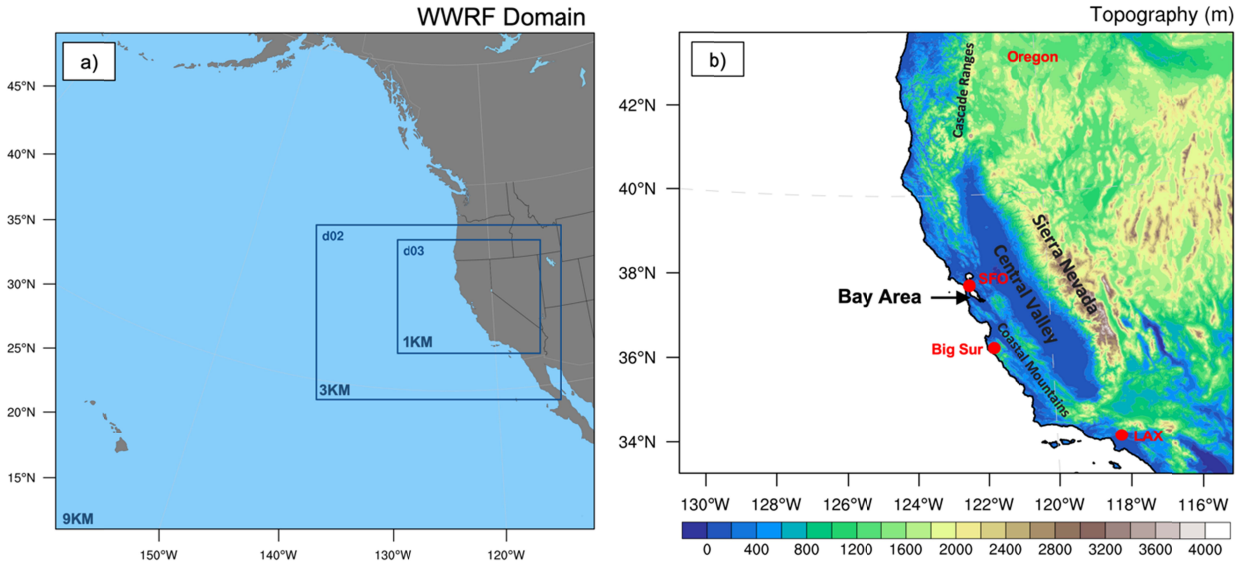


**Figure 2.** Study area of the 2021 January NCFR case. a) Three WWRF domains selected for this study. b) Topography over the study area.

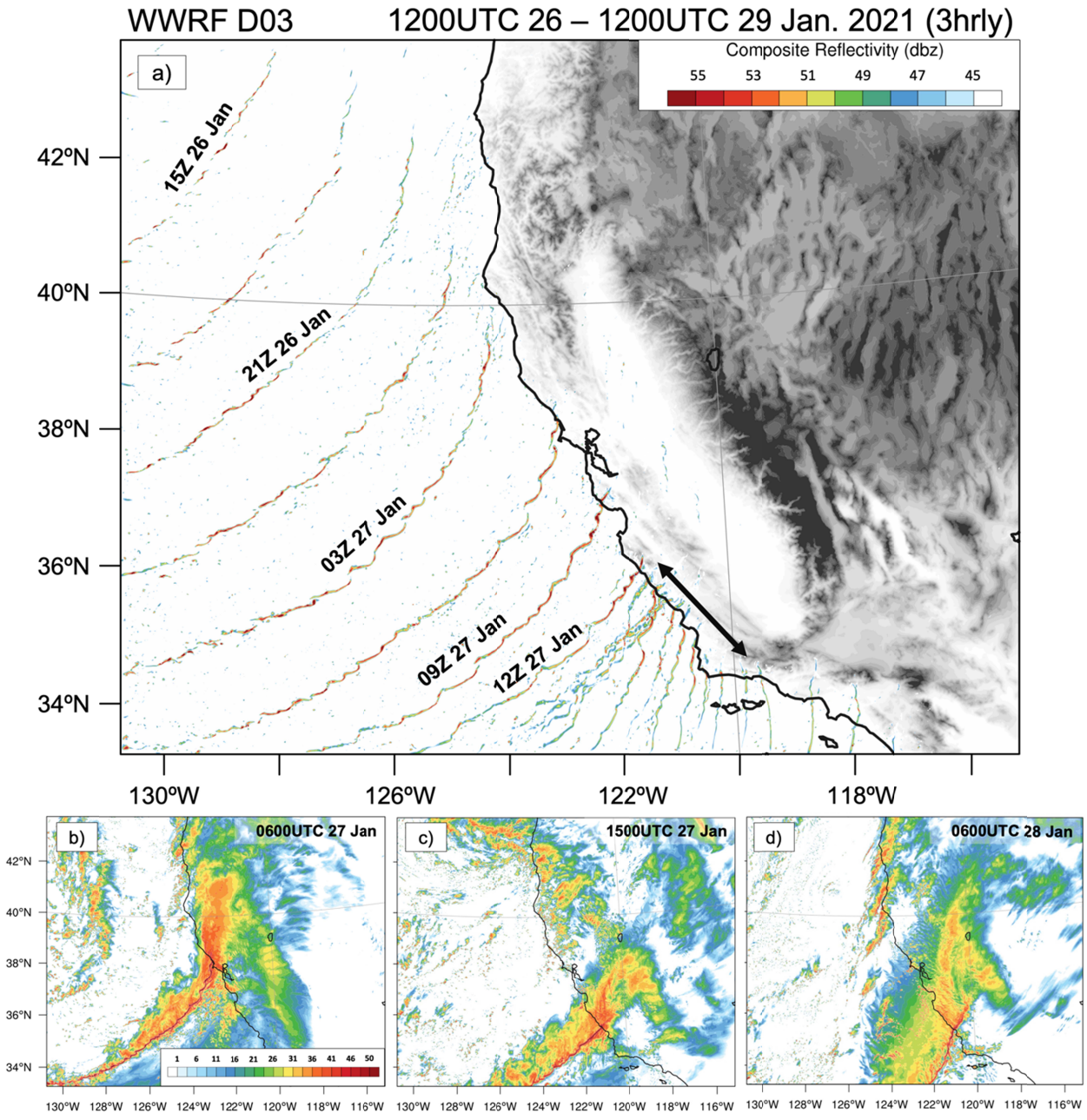


**Figure 3.** Overview of the 2021 January NCFR event. a) Three hourly NCFR positions based on WWRF D03 simulations from 1200UTC 26 to 1200UTC 29 January 2023. b) – d) Composite reflectively from WWRF D03 simulations at 0600UTC 26 January, 1500UTC 27 January, and 0600UTC 28 January.

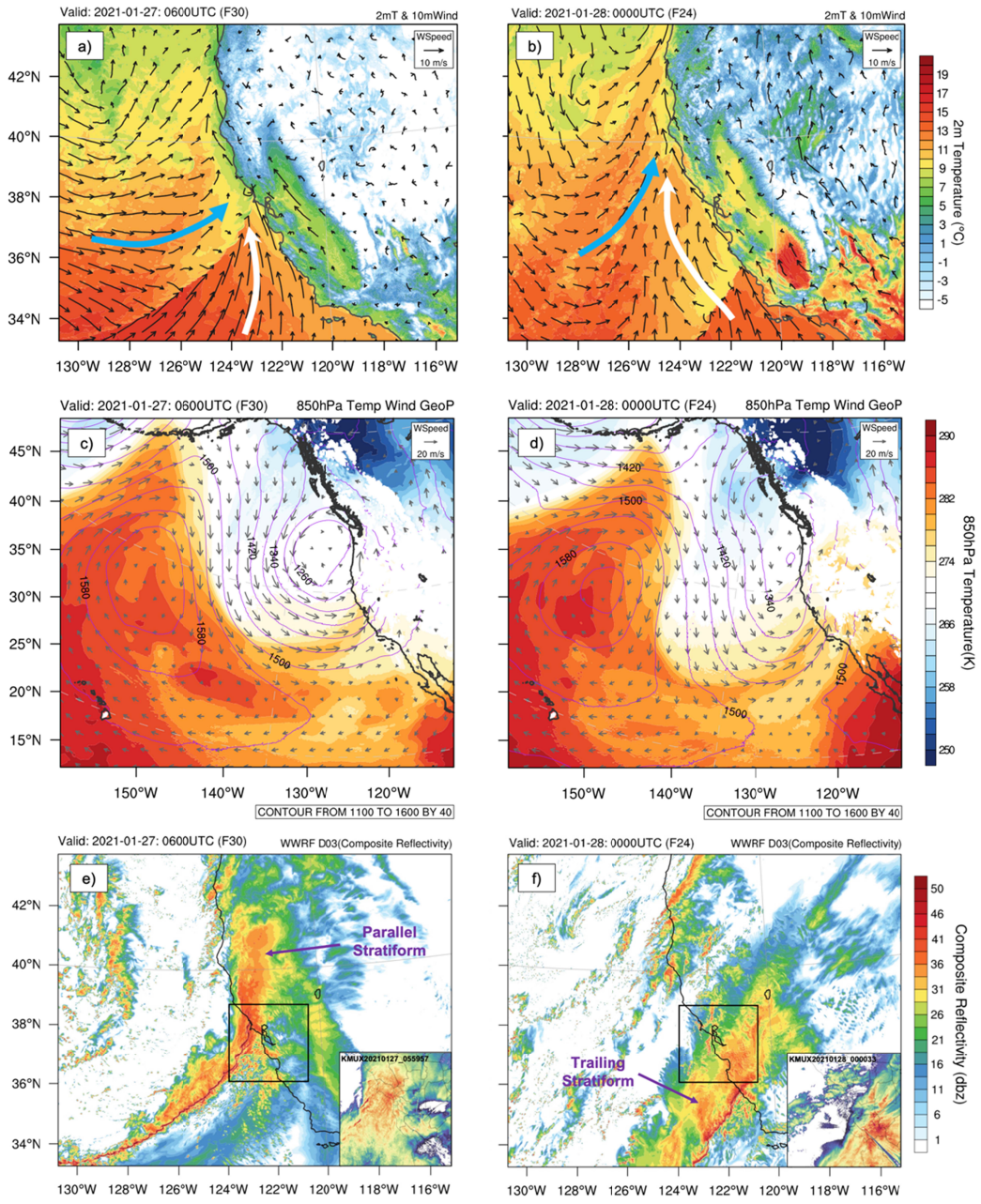


**Figure 4.** Parallel stratiform (PS) precipitation and trailing stratiform (TS) precipitation during the 2021 January NCFR event. a) and b) 2-m temperature and 10-m wind from WWRF D03 (1km) at 0600 UTC 27 January (PS) and 0000 UTC 28 January (TS), respectively. Blue arrow represents cold air advection, and white arrow represents warm air advection. c) and d) 850-hPa geopotential height (contour line), temperature (contour fill), and wind field (vector) from WWRF D01 (9km) at 0600 UTC 27 January and 0000 UTC 28 January, respectively. e) and f) Composite reflectivity from WWRF D03 (1km) at 0600 UTC 27 January and 0000 UTC 28 January, respectively. The subplot at the right corner in c) and d) are NEXRAD observations at San Francisco station (KMUX). Black boxes in c) and d) represent the domain of the subplots.

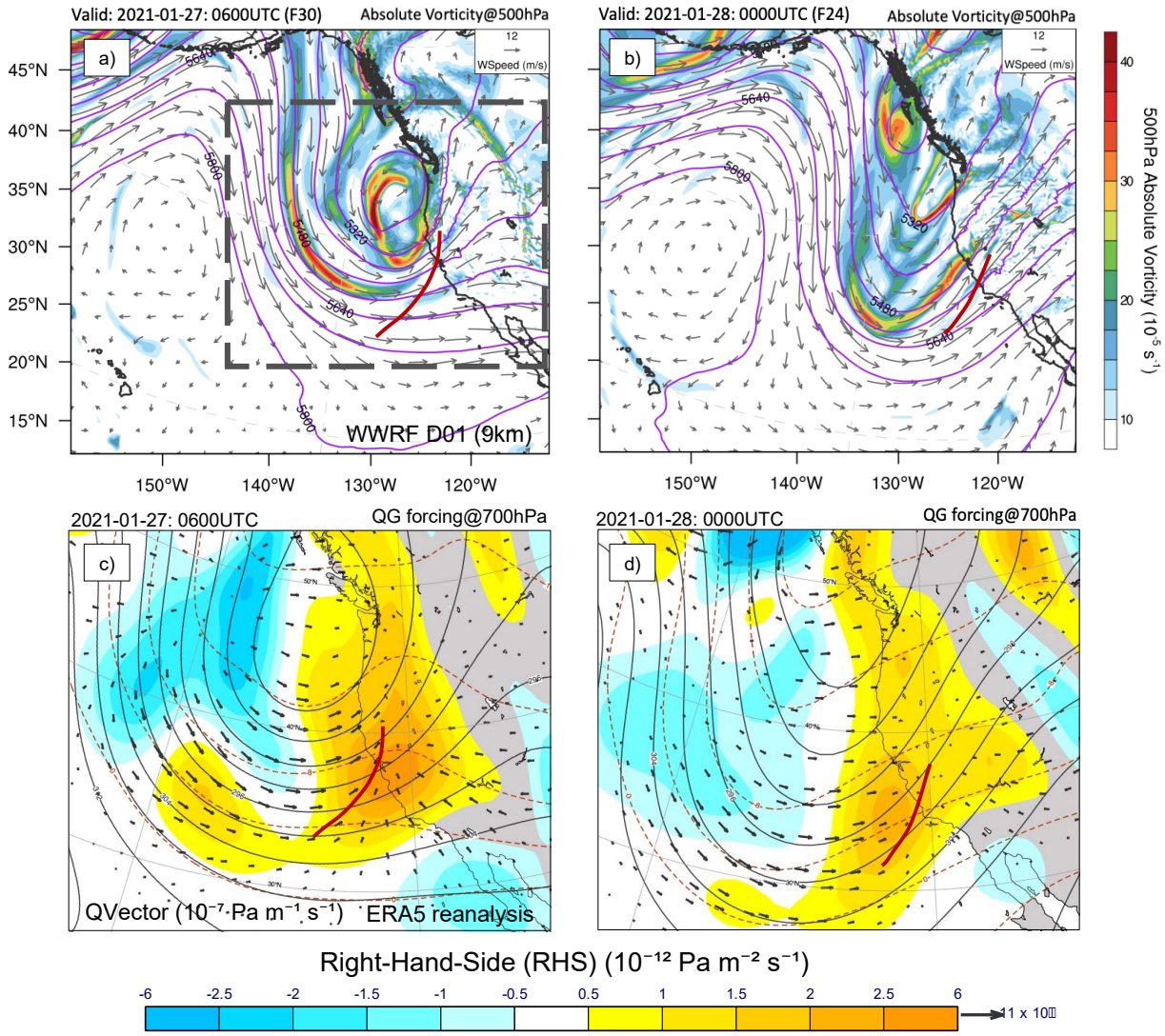


**Figure 5.** Synoptic forcing during both PS and TS precipitation based on WWRF D01 simulations and ERA5 reanalysis data. a) and b) 500hPa absolute vorticity (contour fill), geopotential height (solid purple line), and wind field (vector) at 0600 UTC 27 and 0000 UTC 28 January, respectively. c) and d) 700hPa right-hand-side value calculated based on Omega equation (contour fill), geopotential height (solid black line), and temperature (dashed red line) at 0600 UTC 27 and 0000 UTC 28 January, respectively. The solid red line represents the location of the NCFR. Dashed gray box in a) represents the domain in c) and d).

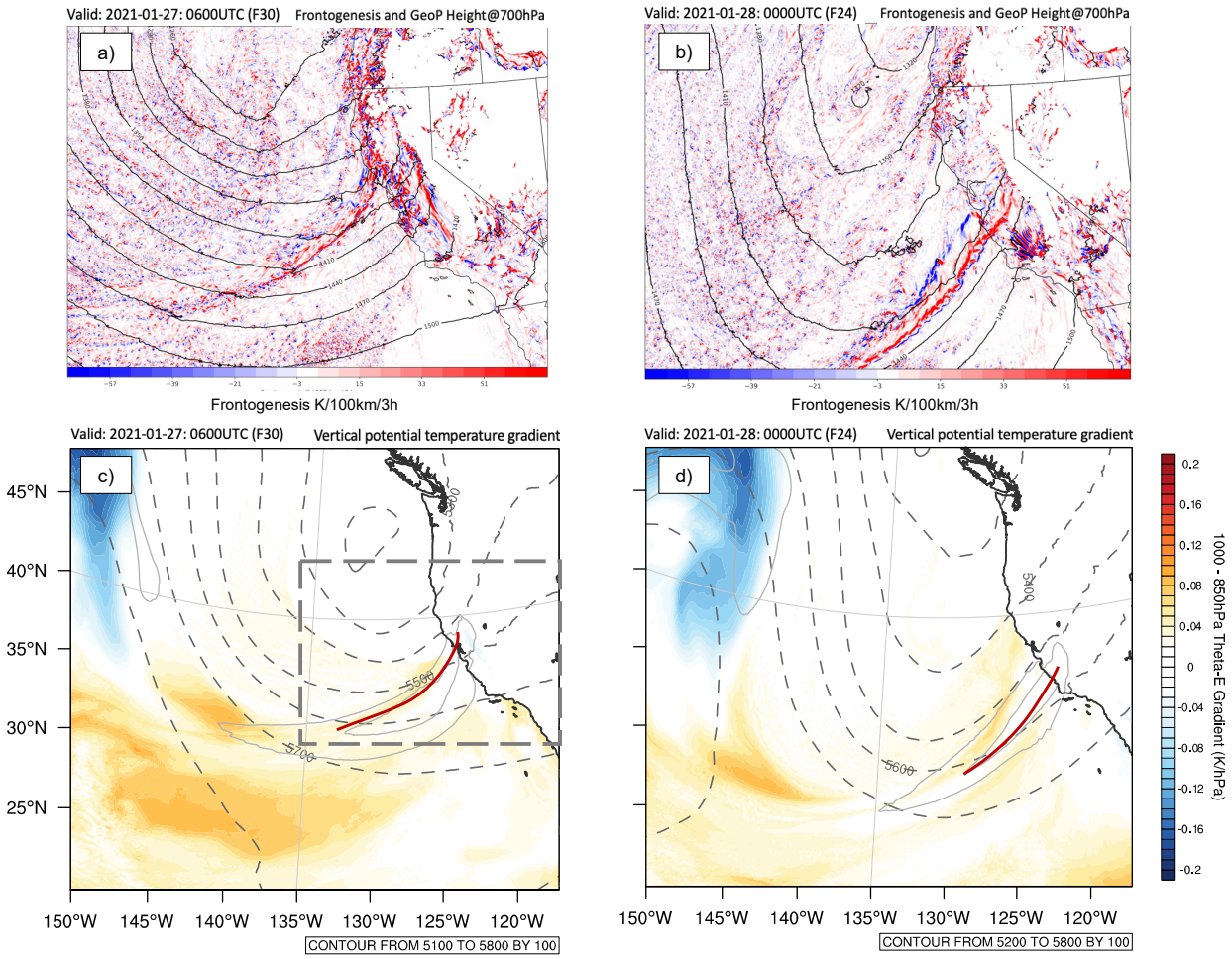


**Figure 6.** Mesoscale forcing during both PS and TS precipitation. a) and b) 700hPa geopotential height (contour line) and frontogenesis (contour fill) from WWRF D02 at 0600UTC 27 January and 0000UTC 28 January, respectively. c) and d) 500hPa geopotential height (contour line) equivalent potential temperature gradient (contour fill) between 850-1000 hPa from WWRF D01 at 0600UTC 27 January and 0000UTC 28 January, respectively. Grey solid lines in c) and d) indicate AR location (IVT > 250 kg $m^{-1}$ $s^{-1}$). Red solid lines in c) and d) indicate the location of NCFR. Grey dashed box in c) represents the domain in a) and b).

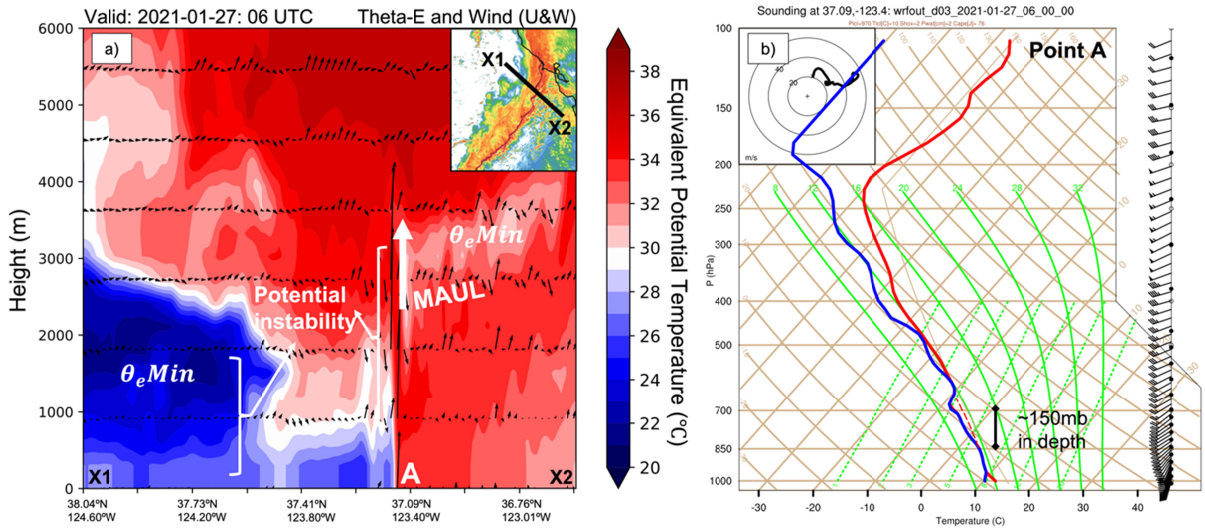


**Figure 7.** Moist absolutely unstable layers (MAUL) captured in WWRF D03 simulations at 0600UTC 27 January 2023. a) Cross-section of equivalent potential temperature and wind (u, w). Subplot at the top right corner is the composite reflectivity with the location of cross-section (black line; X1X2). b) Skew-T plot at location A labeled in a).

539 **Table 1.** WWRF model setting.

| | **WWRF V4.3.1** |
|---|---|
| Input data | ECMWF reanalysis data (ERA5) |
| Horizontal resolution | 9 km / 3 km / 1 km |
| Vertical levels | 100 levels |
| Temporal resolution | 30min |
| Spin-up | 24h |
| Microphysics | Thompson |
| PBL scheme | YSU scheme |
| Shortwave and longwave | Both RRTMG |
| Land surface options | Noah-MP land surface model |
| Surface layer options | Monin-Obukhov Similarity scheme |
| Cumulus options | Grell-Devenyi ensemble scheme |

540

**Table 2.** Observed Total Precipitation Accumulations Compared to Historical Records.

| Location | 2-day Total Accumulations (mm) | Average Recurrence Interval | Max 3-hour Total Accumulations (mm) | Average Recurrence Interval |
|---|---|---|---|---|
| San Cruz, CA | 130.05 | ~7 years | 30.74 | ~2 years |
| Monterey, CA | 79.03 | ~7 years | 25.40 | ~2 years |
| Millers Ranch, CA | 195.83 | ~15 years | 29.97 | ~1.25 years |
| Bryson, CA | 339.60 | ~110 years | 60.96 | ~17 years |
| San Luis Obispo, CA | 107.45 | ~5 years | 22.35 | <1 year |

*2-day total accumulation and max 3-hour total accumulations are from CDEC stations and ASOS stations archived at University of Utah MesoWest dataset (https://mesowest.utah.edu/cgi-bin/droman/download_api2.cgi). Precipitation frequency (PF) is calculated based on frequency analysis of partial duration series (PDS) via NOAA Atlas, Volume 6, Version 2 dataset (https://hdsc.nws.noaa.gov/hdsc/pfds/pfds_map_cont.html). Average recurrence intervals are estimated based on the PF value of 3-hour and 2-day accumulations.